Spacetime Geometric Memory as an Effective Dark Halo

Alejandro Rey
Independent Researcher, Argentina
ORCID: 0009-0007-5052-3917
reyalejandro311@gmail.com

June 27, 2026

Abstract

Weak-field gravity is normally treated as an instantaneous response of geometry to matter. We test a constitutive alternative in which a geometric residual $\mathbf{q}$ relaxes toward the baryonic configuration with a local clock τ_{eff}. The SPARC radial-acceleration scale fixes the galactic benchmark at $\tau_{\text{vac}} = 36.6$ Myr. With this clock held fixed, the theory predicts gas-lensing offsets in nine dissociative cluster mergers ($r = 0.925$), reproduces the isolated GAMA weak-lensing profile ($\chi^2/N = 1.22$), and recovers the environmental dependence of 6dFGSv peculiar velocities ($\Delta\text{AIC} = 54.3$). No parameter is fitted to these three holdouts. A subsequent full-covariance lensing fit measures $A_{\text{rel}} = 1.267 \pm 0.032$ in isolated KiDS lenses. The covariant closure activates this optical excess in nonlinear Weyl curvature while returning $A_{\text{rel}} \simeq 1$ in linear FLRW geometry. A direct CAMB implementation confirms the separation. With the SPARC clock fixed before the cosmological calculation, the native Planck 2018 TT, TE, EE, low-ℓ polarization, and lensing likelihoods give $\chi^2 = 1005.291$ for TIDE and 1005.337 for ΛCDM. Converged chains give $\beta_{\text{tide}} = 1.0128^{+0.0326}_{-0.0356}$ and a finite posterior for the clock evolution. The data thus separate a relaxation clock governing dynamical lag from a curvature-activated optical projection, consistent with part of the effective halo being residual geometry rather than unseen particulate mass alone.

1 Introduction: The Missing Time

In the weak-field quasi-static limit, General Relativity reduces to Poisson's equation. Geometry is solved from the instantaneous matter distribution, with no variable describing how long the response takes. This paper asks what changes if weak-field geometry retains a finite memory of a changing source.

We describe that memory by a residual field $\mathbf{q}$ that relaxes toward the baryonic configuration over a local time τ_{eff}. We call this constitutive framework TIDE. Its defining departure from acceleration-law and emergent-response approaches [1–3] is temporal: systems with the same instantaneous baryonic field can differ because their geometries have had different times to relax.

The proposal separates two observable effects. The relaxation clock controls dynamical lag; the optical coefficient A_{rel} controls how the same residual geometry appears to light. The clock is local rather than universal and may change with environment. The optical excess is activated by nonlinear Weyl curvature and vanishes in the conformally flat linear limit. This separation allows nearby halo phenomenology and the early Universe to test different parts of the same construction.

The empirical strategy is deliberately sequential. SPARC fixes the local galactic clock. That value is then held fixed in three independent tests: cluster-merger offsets, weak lensing, and peculiar velocities. Finally, a direct CAMB implementation confronts the same clock with the native Planck TT, TE, EE, low-ℓ polarization, and lensing likelihoods, followed by a joint TT+BAO+SN+growth analysis. No parameter is fitted to the three cross-scale holdouts. In cosmology, τ_0 remains fixed while its evolution and perturbative response are inferred.

These observables reconstruct gravity, not particle identity. If geometry retains $\mathbf{q}$ after its baryonic source changes, orbital motion and light will map that delayed curvature as an effective halo. The dimensional argument, a covariant torsional realization, sample audits, and numerical implementations are collected in the appendices so that the main text can follow this empirical test directly.

2 A Constitutive Clock for Weak-Field Gravity

2.1 Memory and relaxation

Define the residual between the inferred and baryonic fields by

$$\mathbf{q} \equiv \mathbf{g}_{\rm eff} - \mathbf{g}_{\rm bar}. \tag{1}$$

The minimal causal relaxation law is

$$\tau \frac{D\mathbf{q}}{Dt} + \mathbf{q} = \mathbf{q}_{\rm eq}(\mathbf{g}_{\rm bar}), \qquad \mathbf{g}_{\rm eff} = \mathbf{g}_{\rm bar} + \mathbf{q}. \tag{2}$$

Here $\mathbf{q}$ is not an added matter density. It is the coarse-grained geometric response that remains after the instantaneous baryonic field is removed.

For $\tau \to 0$, $\mathbf{q}$ follows its equilibrium value instantaneously. Newtonian gravity is recovered where that equilibrium residual also vanishes. At finite τ, the relevant control variable is the Deborah number

$$\mathrm{De} \equiv \frac{\tau_{\rm eff}}{t_{\rm dyn}}. \tag{3}$$

The clock is local. In the overdamped torsional realization of Appendix A,

$$\tau_{\rm eff}(x,t) = \frac{\Gamma_S[\mathcal{I}(x,t)]}{m_S^2[\mathcal{I}(x,t)]}, \tag{4}$$

where $\mathcal{I}$ denotes the local environment. The value inferred from SPARC is therefore a galactic benchmark, not a universal constant.

2.2 The relaxed galactic limit

For a relaxed galaxy, Eq. (2) reduces to an equilibrium closure. We use the quadratic radial-acceleration form

$$g_{\rm obs}(g_{\rm bar}) = \frac{1}{2}\left[g_{\rm bar} + \sqrt{g_{\rm bar}^2 + 4a_0 g_{\rm bar}}\right], \tag{5}$$

with

$$q_{\rm eq}(g_{\rm bar}) = g_{\rm obs} - g_{\rm bar}. \tag{6}$$

This closure specifies the equilibrium target; the constitutive content is the finite-time evolution toward it.

2.3 What light measures

If $\mathbf{q}$ is geometric, massive tracers and light must respond to the same residual metric. Dynamics measures its temporal potential U, while lensing measures the corresponding Weyl potential. We write the observable weak-lensing projection as

$$g_{\rm lens} = g_{\rm bar} + A_{\rm rel}\, q(g_{\rm bar}), \qquad A_{\rm rel} = \beta_{\rm W}, \tag{7}$$

where β_{W} is the spatial-to-temporal response of the residual metric. Its minimal bounded curvature dependence is

$$A_{\mathrm{rel}}(\mathcal{W}) = 1 + \alpha_{\mathrm{W}} \frac{\mathcal{W}}{1+\mathcal{W}}, \tag{8}$$

with $\mathcal{W}$ the ratio of tidal Weyl curvature to local isotropic Ricci curvature. Hence $A_{\mathrm{rel}} \to 1$ in linear FLRW geometry and approaches $1 + \alpha_{\mathrm{W}}$ in a nonlinear halo. Appendix D derives the covariant metric closure, the equivalent anisotropic stress, and the CAMB implementation.

3 Measuring the Local Weak-Field Clock in SPARC

SPARC fixes the relaxed weak-field benchmark. Its empirical RAR scale, $a_0 = 1.2 \times 10^{-10}\,\mathrm{m\,s^{-2}}$ [4, 5], maps to the constitutive clock through

$$a_0 = \frac{V_*}{\tau_{\mathrm{vac}}}, \tag{9}$$

Taking $V_* = \langle V_{\mathrm{flat}} \rangle = 138.5$ km s^{-1} over the $N = 129$ high- and medium-quality systems gives

$$\tau_{\mathrm{vac}} \simeq 36.6 \text{ Myr}. \tag{10}$$

The 6.2 km s^{-1} jackknife error on the sample mean gives $\tau_{\mathrm{vac}} = 36.6 \pm 1.6$ Myr at fixed a_0; a 20,000-draw bootstrap gives the consistent 68% interval 35.0–38.2 Myr. The same closure organizes all 3389 kinematic points in the full 175-galaxy sample with an RMS scatter of 0.205 dex.

Equation (9) interprets the established equilibrium scale as a clock. Its predictive content is tested only after this clock leaves the SPARC sample and is held fixed in the independent observations below.

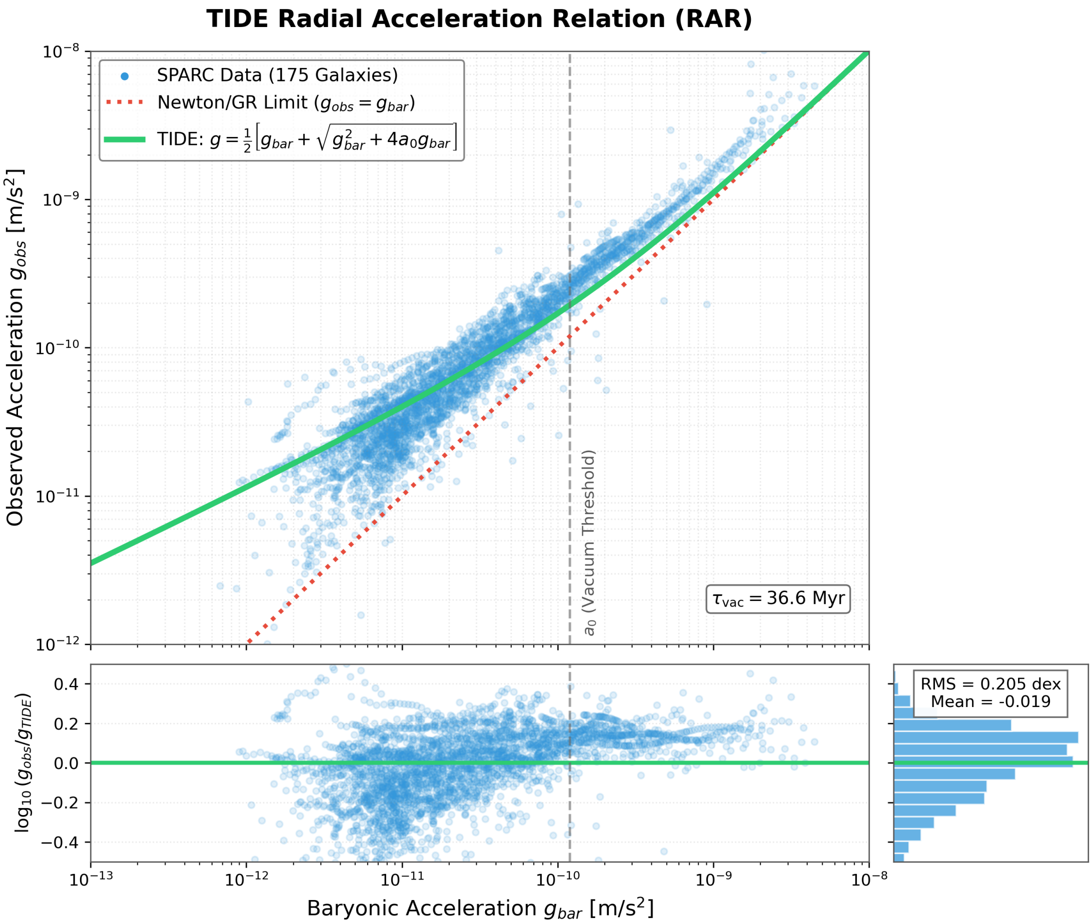

Figure 1: SPARC radial-acceleration relation and residual distribution for 175 galaxies (3389 kinematic points). The fixed closure gives an RMS scatter of 0.205 dex.

4 Blind Cross-Scale Tests

The three tests translate geometric memory into three observables: displaced lensing mass, halo-like weak-lensing shear, and excess peculiar motion. Each is evaluated after the SPARC clock and equilibrium closure are frozen. No cluster clock, lensing normalization, halo mass, or dataset-specific TIDE parameter is fitted. The later covariance measurement of $A_{\rm rel}$ diagnoses the optical projection and does not enter the zero-refit lensing holdout.

4.1 CLUSTER MERGERS: time becomes distance

Dissociative cluster mergers give the most direct spatial-lag test. In a merger, the baryonic source distribution changes on a finite timescale. If weak-field geometry relaxes with delay, the residual curvature should lag behind the collisional gas and be reconstructed by lensing as a displaced effective halo.

The constitutive prediction is dimensional and zero-refit:

$$d_{\rm pred} = v_{\rm col}\,\tau_{\rm vac}. \tag{11}$$

The nine-system sample was fixed before evaluation by requiring a resolved subcluster-scale gas–lensing offset, a usable literature collision velocity, and a common offset definition across systems; the complete selection audit is given in Appendix B. For the same-definition nine-cluster sample, this gives

$$r = 0.925, \qquad p = 3.5\times10^{-4}, \qquad \langle d_{\rm obs}/d_{\rm pred}\rangle = 1.31 \pm 0.10. \tag{12}$$

With propagated velocity uncertainty the fixed-τ prediction gives $\chi^2/\mathrm{dof} = 1.82$, compared with 3.99 for a constant-offset null.

Table 1: Audited same-definition merger observables entering the blind offset test. Velocities are in km s^{-1} and offsets in kpc; source references and selection details are given in Appendix B. The prediction uses $\tau_{\mathrm{vac}} = 36.6$ Myr fixed from SPARC.

Cluster	v_{col}	d_{obs}	σ_d	d_{pred}	$d_{\mathrm{obs}}/d_{\mathrm{pred}}$
Bullet 1E0657	3000	150	25	112.3	1.336
El Gordo ACT J0102	2250	130	20	84.2	1.544
MACS J0025	2000	90	15	74.9	1.202
Abell 520	2300	100	20	86.1	1.162
ZwCl 0008	1100	42	12	41.2	1.020
Abell 2146	2000	120	20	74.9	1.602
Abell 1758N	1500	90	15	56.1	1.603
Abell 115	1600	85	15	59.9	1.419
A3667	1100	45	10	41.2	1.092

This is the observational meaning of geometric memory in its most direct form: a temporal relaxation scale becomes a spatial offset. Delayed curvature would be reconstructed as a displaced dark halo.

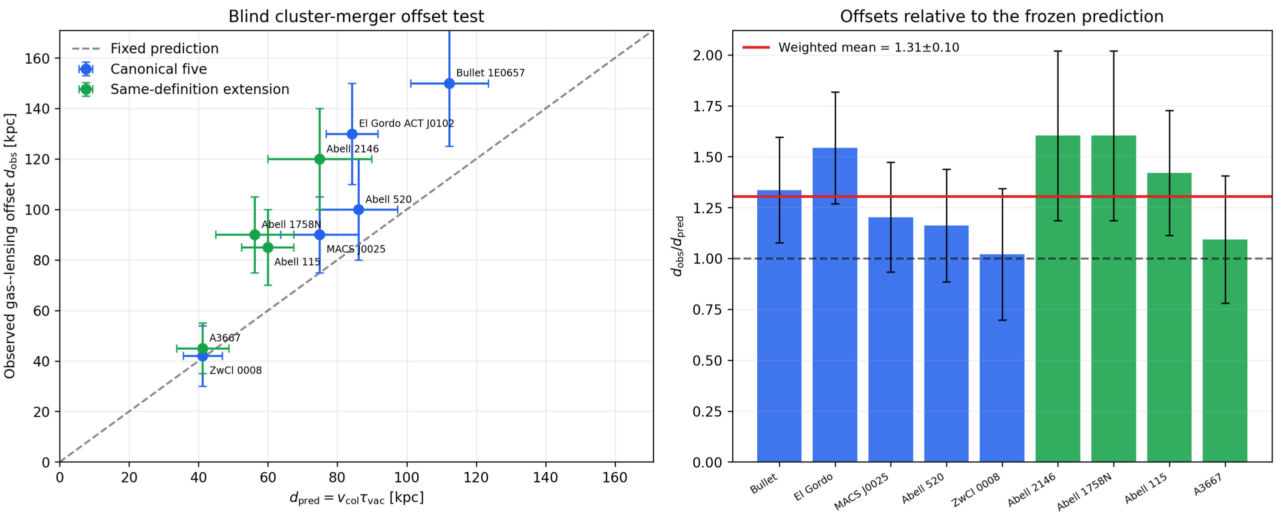

Figure 2: Blind cluster-merger offset test for the audited nine-system sample. Left: observed offsets against the fixed-SPARC prediction; the dashed line denotes exact agreement. Right: individual ratios, with the red line showing the weighted mean 1.31 ± 0.10. Blue and green identify the canonical and same-definition extension subsets.

4.2 WEAK LENSING: light sees the residual

Weak lensing directly reconstructs gravitational geometry rather than the orbital response of a tracer population. If the residual $\mathbf{q}$ is geometric, its contribution should appear in lensing as an effective excess surface density.

The GAMA isolated weak-lensing sample gives $\chi^2/N = 1.22$ (PTE $= 0.25$) for the fixed SPARC closure, compared with $\chi^2/N = 6.51$ for baryons alone. The KiDS isolated sample carries stronger environmental contamination but still rejects the baryonic-only null: $\chi^2/N = 7.75$ versus 110.60.

The full Brouwer et al. covariance also isolates the relativistic projection. The KiDS sample gives

$$A_{\rm rel} = 1.267 \pm 0.032, \qquad \Delta A_{\rm rel} \equiv A_{\rm rel} - 1 = 0.267 \pm 0.032, \tag{13}$$

an 8.5σ departure from the scalar value $A_{\rm rel} = 1$; GAMA gives $A_{\rm rel} = 1.145 \pm 0.127$. Through Eq. (7), the KiDS measurement corresponds to

$$\beta_{\rm W}^{\rm KiDS} = 1.267 \pm 0.032, \qquad \left.\frac{\Phi_q}{\Psi_q}\right|_{\rm KiDS} = 2\beta_{\rm W}^{\rm KiDS} - 1 = 1.535 \pm 0.063. \tag{14}$$

The zero-refit holdout above uses $A_{\rm rel} = 1$; this subsequent fit measures how the residual projects into light and does not alter that prediction.

The four isolated KiDS stellar-mass bins provide an internal activation check. Their amplitudes are 1.092 ± 0.085, 1.314 ± 0.069, 1.298 ± 0.058, and 1.292 ± 0.048 from low to high mass. A joint full-covariance fit to the upper three bins gives the saturated response

$$\alpha_{\rm W} = 0.295 \pm 0.034, \qquad A_{\rm rel}^{\rm sat} = 1.295 \pm 0.034. \tag{15}$$

The lowest-mass bin differs from this plateau at 2.26σ after the published cross-bin covariance is propagated. Stellar mass is not itself the invariant $\mathcal{W}$, but the observed rise and saturation have the sign predicted by Eq. (8).

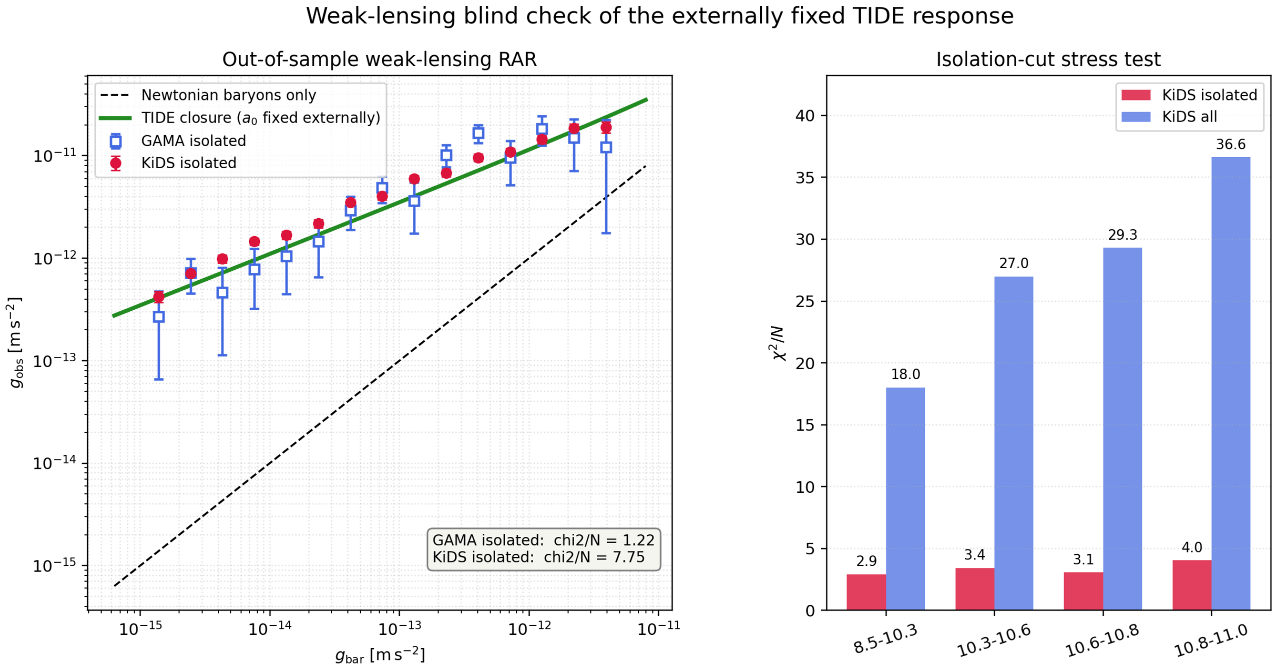

Figure 3: Weak-lensing holdout. Left: the fixed-SPARC closure against the isolated GAMA and KiDS acceleration profiles. Right: degradation after removing the isolation cut.

4.3 PECULIAR VELOCITIES: environment carries memory

Peculiar velocities test the temporal character of the framework rather than another acceleration curve. In low-density or dynamically younger environments, the relevant systems have completed fewer local dynamical times relative to their relaxation state. TIDE therefore predicts larger residual velocity dispersion in the lowest-density environments.

Using the 6dFGSv galaxy-level sample with $D_H = 40$–200 Mpc and $\epsilon_d < 0.13$ gives $N = 5292$. The dispersion ratio between the lowest- and highest-density quartiles is

$$\sigma(Q_1)/\sigma(Q_4) = 1.232\,[1.206, 1.260] \tag{16}$$

at $R = 8$ Mpc, with Mann–Whitney $p = 6.5 \times 10^{-32}$. The signal survives distance and quality controls:

$$\beta(\log n_8) = -0.1436, \qquad p = 6.2 \times 10^{-14}, \qquad \Delta\mathrm{AIC} = 54.3. \tag{17}$$

The sign follows from the relaxation state encoded by $\mathrm{De} = \tau_{\mathrm{eff}}/t_{\mathrm{dyn}}$. Standard ΛCDM assembly bias can produce a similar environmental trend, so final discrimination requires matched survey mocks. Here the signal has the predicted sign and survives the distance, quality, and environmental controls.

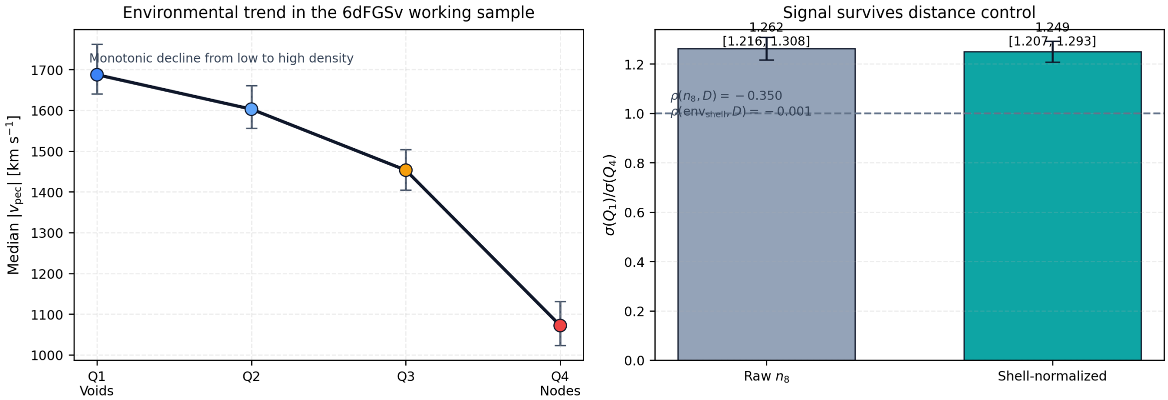

Figure 4: 6dFGSv environmental test for the $N = 5292$ working sample. Left: median $|v_{\mathrm{pec}}|$ across density quartiles. Right: untrimmed raw and shell-normalized dispersion ratios; the headline $R = 8$ Mpc result in the text uses the stated 5% robust tail trim.

5 Native Planck Cosmology with the SPARC Clock Fixed

The low-redshift tests probe geometric memory after nonlinear structure has formed. Cluster offsets and peculiar velocities test temporal lag, while weak lensing also measures the nonlinear optical projection. Linear cosmology probes the complementary limit: the FLRW background is conformally flat, and the Weyl–torsion activation operator contributes only beyond linear order, so $A_{\mathrm{rel}} \to 1$. Planck therefore isolates whether the temporal response can be continued consistently to high redshift without importing the halo-regime optical enhancement.

The SPARC value is not imposed as a universal relaxation time at recombination. It fixes the present-day normalization of

$$\tau_{\mathrm{eff}}(a) = \tau_0 a^p, \tag{18}$$

where τ_0 remains frozen while p and β_{tide} determine the cosmological evolution and perturbative response. The test is therefore externally anchored rather than parameter-free.

5.1 Full TT/TE/EE and lensing likelihood

The primary cosmological test inserts the low-redshift clock into the linear Einstein–Boltzmann system without CMB recalibration. We fix

$$\tau_0 = 11.22 \text{ Mpc}/c = 36.6 \text{ Myr} \tag{19}$$

before evaluating low-ℓ TT, SROLL2 low-ℓ EE, high-ℓ Plik-lite TTTEEE, and the reconstructed lensing potential. Both branches use the same CAMB 1.6.7 source tree and standard cosmological assumptions; TIDE adds only the evolution index p and perturbative response β_{tide}. The sampling configuration and convergence audit are given in Appendix F.

A profile-likelihood minimization initialized from the corresponding chains gives

$$\chi^2_{\mathrm{TIDE}} = 1005.291, \qquad \chi^2_{\Lambda\mathrm{CDM}} = 1005.337, \qquad \Delta\chi^2 = -0.046. \tag{20}$$

The two descriptions reach the same CMB likelihood surface. The clock is fixed outside cosmology yet reaches the native temperature, polarization, and lensing optimum without adjustment.

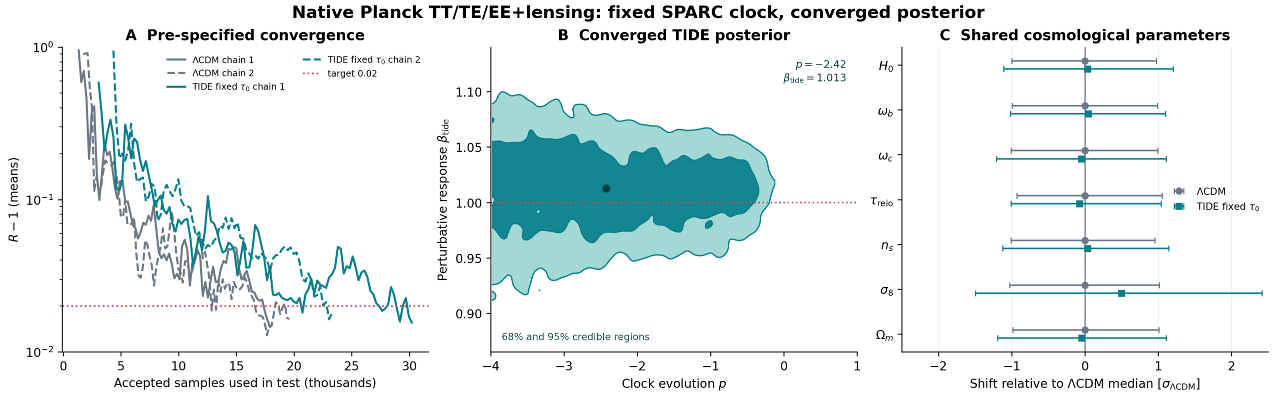

Figure 5: Converged native-Planck posterior with the SPARC clock fixed before sampling. Left: the four chains cross the pre-specified Cobaya $R - 1 = 0.02$ stopping threshold. Centre: the 68% and 95% credible regions for the clock-evolution index p and perturbative response β_{tide}. Right: posterior-mean shifts of the shared cosmological parameters relative to ΛCDM, all below 0.19σ.

Table 2: Native Planck 2018 profile-likelihood minima. The relaxation clock is fixed to the SPARC value in the TIDE branch. Absolute block values include likelihood normalization constants; row differences within the same block carry the model comparison.

Model	low-ℓ TT	low-ℓ EE	TTTEEE	Lensing	Total
ΛCDM	23.269	390.064	583.184	8.821	1005.337
TIDE fixed	23.529	389.983	582.984	8.796	1005.291

The TIDE minimum lies at

$$p = -0.895, \qquad \beta_{\mathrm{tide}} = 1.0069, \tag{21}$$

with $H_0 = 67.31\ \mathrm{km\,s^{-1}\,Mpc^{-1}}$ and $\sigma_8 = 0.818$. The converged fixed-clock posterior gives

$$p = -2.424^{+1.343}_{-1.094}, \qquad \beta_{\mathrm{tide}} = 1.0128^{+0.0326}_{-0.0356} \quad (68\%), \tag{22}$$

with 95% intervals $-3.923 < p < -0.475$ and $0.9392 < \beta_{\mathrm{tide}} < 1.0791$. The lower tail of p approaches the prior boundary at -4. A likelihood slice extended to $p = -8$ changes χ^2 by less than 0.27: Planck favors $p < 0$ but leaves its lower bound and median prior-dependent. By contrast, β_{tide} is centred on unity; their posterior correlation is only -0.016. All four chains terminated automatically under the pre-specified Cobaya criteria, with final $R - 1 = 0.0146$–0.0180. The shared cosmological posterior means move by at most 0.19σ relative to ΛCDM.

Planck alone therefore does not prefer the two additional TIDE parameters by AIC ($\Delta\mathrm{AIC} = +3.954$). It establishes the stronger result needed here: the externally calibrated clock occupies a finite converged posterior region while preserving the acoustic, polarization, and lensing structure. This implementation retains CAMB's standard CDM background bookkeeping and tests the constitutive dynamics; replacing that sector by a covariantly derived q stress–energy is a separate calculation.

5.2 Cross-probe likelihood with the SPARC clock fixed

The same fixed-clock branch is next tested against 83 binned Planck TT points, 12 DESI BAO entries, 1580 Pantheon+ supernovae, and eight $f\sigma_8$ measurements. This is a cross-probe consistency test; the primary CMB comparison remains the native Planck likelihood of Section 5.1. Its construction is documented in Appendix G.

Relative to vanilla ΛCDM, the sampled joint likelihood improves by $\Delta\chi^2 = -11.92$ with two additional parameters. This gives $\Delta\mathrm{AIC} = -7.92$ and $\Delta\mathrm{BIC} = +2.94$: the likelihood gain exceeds the AIC penalty, while the stricter BIC retains a modest preference for the lower-dimensional model. In both criteria, τ_0 remains fixed to SPARC rather than fitted to cosmology.

Table 3: Joint cross-probe model comparison. Differences are quoted relative to vanilla ΛCDM; negative $\Delta\chi^2$ and ΔAIC favor TIDE.

Model	Treatment of τ_0	k	χ^2	$\Delta\chi^2$	ΔAIC	ΔBIC
ΛCDM	—	5	1491.54	0.00	0.00	0.00
TIDE fixed	SPARC: 11.22 Mpc/c	7	1479.63	−11.92	−7.92	+2.94

For the fixed-SPARC branch, the evolving clock and perturbative coupling are constrained to

$$p = -1.395^{+0.577}_{-0.703}, \qquad \beta_{\mathrm{tide}} = 1.192^{+0.060}_{-0.054}. \tag{23}$$

This intermediate value lies about 2.7σ above the native-Planck centre. Compressed TT data and weaker convergence prevent treating it as a second native measurement; resolution requires a native joint likelihood. Its numerical proximity to the halo weak-lensing amplitude originally motivated a direct identification with β_{W}. The completed Einstein-equation test separates the two channels. The parameter β_{tide} controls the clustering-source response in Eq. (51); β_{W} controls the anisotropic optical stress in Eq. (44). They are not the same universal coefficient.

Implementing the covariant optical stress directly in CAMB gives

$$\beta_{\mathrm{W}}^{\mathrm{linear}} = 1.00081, \qquad 0.99769 < \beta_{\mathrm{W}}^{\mathrm{linear}} < 1.00396 \quad (\Delta\chi^2_{\mathrm{TT}} \leq 1). \tag{24}$$

The $\beta_{\mathrm{W}} = 1$ limit recovers the previous solver to 1.9×10^{-7} in χ^2_{TT}. Applying the halo value $A_{\mathrm{rel}} = 1.267$ as an unscreened linear coefficient instead gives $\Delta\chi^2_{\mathrm{TT}} = 6669$. The full calculation therefore selects the curvature-activated closure of Eq. (8): no more than 1.34% of the saturated halo optical response may leak into the linear CMB regime at $\Delta\chi^2 = 1$. Appendix D gives the field-equation insertion and numerical audit.

The block decomposition localizes the result: Planck TT drives most of the gain, BAO also improves, Pantheon+ remains comparable, and the compact $f\sigma_8$ block favors the vanilla realization. Growth is therefore the next discriminating observable for the fixed-clock extension. Chain diagnostics and blockwise χ^2 values are reported in Appendix G.

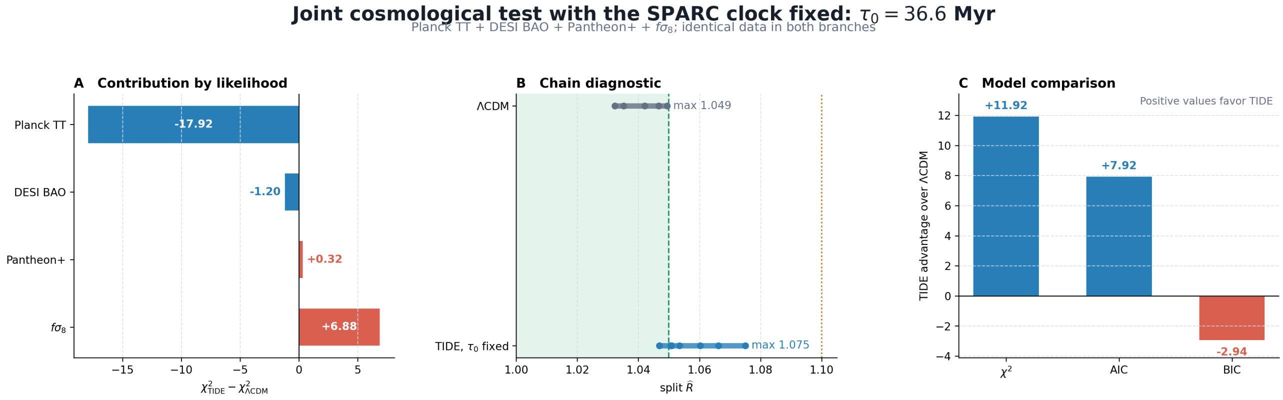

Figure 6: Joint cosmological test with the SPARC relaxation clock fixed. Panel A decomposes $\chi^2_{\rm TIDE} - \chi^2_{\Lambda\rm CDM}$ by likelihood block. Panel B reports the split-$\widehat{R}$ range of the extended chains. Panel C compares the gains in χ^2, AIC, and BIC; positive values favor TIDE under the sign convention shown.

6 Discussion: Effective Halos as Delayed Geometry

The three holdouts probe the same physical distinction in different ways. A merger converts temporal lag into distance, weak lensing tests whether light sees the residual, and peculiar velocities test whether the response depends on environment. Their common scale was fixed before any of these data were evaluated.

This changes the operational meaning of an inferred halo. Standard analyses map the difference between baryonic matter and reconstructed gravity into an unseen mass distribution. Here the same difference can be carried by $\mathbf{q}$: geometry that has not relaxed to the current baryonic configuration. Particle dark matter and delayed curvature are therefore observationally degenerate in part of the nonlinear weak-field regime. The discriminating prediction is temporal: the inferred excess must track relaxation state, not baryonic acceleration alone.

The lensing and CMB results further separate the response into a local clock and a curvature-dependent optical projection. Nonlinear Weyl geometry activates the measured halo amplitude, while linear FLRW geometry selects $A_{\rm rel} \simeq 1$. The native Planck result shows that this separation preserves the acoustic, polarization, and lensing likelihood surface when the local clock is carried into cosmology without recalibration.

7 What Would Falsify TIDE

Four observations can directly reject the framework:

1. the relation $d \propto v_{\rm col}\tau$ disappears in a larger same-definition merger sample;
2. controlled lensing data fail to recover the residual field or its transition from $A_{\rm rel} \simeq 1$ in linear geometry to a saturated halo value;
3. the peculiar-velocity dependence on environment disappears after distance and selection controls; or
4. a full Planck+BAO+LSS likelihood requires a clock incompatible with the SPARC benchmark under every coherent $\tau_{\rm eff}(a)$ evolution.

The existing CMB calculation already bounds leakage of the saturated halo optical response into the linear regime to 1.34% at $\Delta\chi^2 = 1$.

8 Conclusion

SPARC fixes a local weak-field clock at $\tau_{\mathrm{vac}} = 36.6$ Myr. Without refitting it, cluster mergers recover the predicted spatial lag, weak lensing recovers the residual field, and peculiar velocities recover its environmental signature. Lensing then measures the distinct optical response, $A_{\mathrm{rel}} = 1.267 \pm 0.032$, while the covariant CAMB implementation suppresses that excess in linear geometry. With the clock still fixed, native Planck TT/TE/EE+lensing gives $\Delta\chi^2 = -0.046$ relative to ΛCDM. The converged posterior centres β_{tide} on unity and shifts every shared cosmological parameter by less than 0.19σ. It favors $p < 0$ while leaving the negative tail prior-limited.

The result is a compact empirical pattern: one locally measured clock organizes independent dynamical, lensing, environmental, and cosmological observables without a system-by-system halo fit. A full native Planck+BAO+LSS posterior is the next test. The present evidence supports the physical possibility that part of the effective weak-field halo is residual geometry, still relaxing toward the baryonic source.

Data and Code Availability

The scripts, datasets, configured CAMB files, and reproduced figures are provided in the accompanying reproducibility package: `https://doi.org/10.5281/zenodo.20894126`.

Acknowledgements and Author Statement

The author thanks the open astronomical-data community and the developers of the public numerical tools used in the reproducibility package. This research was conducted independently, without institutional funding or dedicated computing allocation. AI-assisted tools (Codex and Claude Code) supported code development and auditing, editorial iteration, and consistency checks. The central hypothesis, scientific interpretation, methodological decisions, verification of the reported results, and conclusions are the sole responsibility of the author. This manuscript is intended to make the constitutive-relaxation hypothesis explicit, reproducible, and available for independent testing, extension, and falsification.

A Dimensional and Microscopic Foundation

The constitutive law has two supporting routes: a minimal dimensional argument and an explicit covariant torsional realization [6–8].

A.1 Dimensional necessity

Consider the most general local derivative extension obtained by adding the n-th time derivative of the residual field,

$$f\frac{D^n\mathbf{q}}{Dt^n} + \mathbf{q} = \mathbf{q}_{\rm eq}. \tag{25}$$

Since $[\mathbf{q}] = \mathrm{L\,T}^{-2}$, dimensional consistency requires $[f] = \mathrm{T}^n$. The case $n = 0$ only rescales equilibrium. The case $n = 1$ introduces one timescale and gives the minimal single-channel causal relaxation law; $n \geq 2$ introduces additional initial data and permits oscillatory response. The first-order extension is therefore

$$\tau\frac{D\mathbf{q}}{Dt} + \mathbf{q} = \mathbf{q}_{\rm eq}. \tag{26}$$

This argument fixes the role and dimension of τ, not its value.

A.2 Torsional realization

In ordinary Einstein–Cartan theory, torsion is algebraically tied to the spin density of matter and does not carry independent relaxation dynamics. A propagating memory mode requires an effective extension in which the torsion trace vector

$$S_\mu \equiv T^\lambda{}_{\lambda\mu} \tag{27}$$

is promoted to a massive dynamical field. The minimal local action is of Proca type,

$$\mathcal{S}_T = \int d^4x\sqrt{-g}\left[-\frac{1}{4}F_{\mu\nu}F^{\mu\nu} + \frac{1}{2}m_S^2 S_\mu S^\mu + S_\mu J^\mu\right], \qquad F_{\mu\nu} = \nabla_\mu S_\nu - \nabla_\nu S_\mu, \tag{28}$$

where J^μ is an effective matter/curvature source. Here m_S denotes the infrared effective mass coefficient of the coarse-grained torsional response. No numerical particle mass is inferred, and the present EFT does not identify S_μ with an additional asymptotic particle species. This propagating mode alone is not enough: a conservative massive vector oscillates rather than relaxes. Dissipation is represented by a covariant Rayleigh–Onsager functional,

$$W_{\rm diss} = \int d^4x\sqrt{-g}\,\frac{\Gamma_S}{2}(u^\alpha\nabla_\alpha S^\mu)(u^\beta\nabla_\beta S_\mu), \tag{29}$$

with u^α the coarse-grained baryonic four-velocity. The resulting open-system field equation is a damped Proca equation,

$$\nabla_\nu F^{\mu\nu} + m_S^2 S^\mu + \Gamma_S(u^\alpha\nabla_\alpha)S^\mu = J^\mu. \tag{30}$$

In the infrared overdamped regime, $\omega \ll \Gamma_S$ and $k \ll m_S$, this reduces to

$$\Gamma_S\dot{S}_\mu + m_S^2 S_\mu \simeq J_\mu, \qquad \tau_S\dot{S}_\mu + S_\mu \simeq \frac{J_\mu}{m_S^2}, \qquad \tau_S = \frac{\Gamma_S}{m_S^2}. \tag{31}$$

Identifying the weak-field residual as $\mathbf{q} = \beta\mathbf{S}$ gives Eq. (2) at leading infrared order.

The coefficients may depend on local matter and curvature invariants, making their quotient the field-dependent clock of Eq. (4); a catalogue mass such as M_{500} is only a proxy for that environment. This infrared realization fixes neither m_S, Γ_S, nor β separately and is not a UV completion.

B Cluster Sample and Offset Audit

Table 4 lists the nine dissociative mergers used in Section 4.1. The first five form the canonical subset; the final four are included because the literature reports the same subcluster-scale gas-lensing offset observable with usable collision velocities.

Table 4: Same-definition cluster-merger sample. The prediction is $d_{\rm pred} = v_{\rm col}\tau_{\rm vac}$ with $\tau_{\rm vac} = 36.6$ Myr and no cluster-level fit.

Cluster	$v_{\rm col}$ [km/s]	$d_{\rm obs}$ [kpc]	σ_d [kpc]	$d_{\rm pred}$ [kpc]	$d_{\rm obs}/d_{\rm pred}$	Reference
Bullet 1E0657	3000	150.0	25	112.3	1.336	[9, 10]
El Gordo ACT J0102	2250	130.0	20	84.2	1.544	[11, 12]
MACS J0025	2000	90.0	15	74.9	1.202	[13]
Abell 520	2300	100.0	20	86.1	1.162	[14, 15]
ZwCl 0008	1100	42.0	12	41.2	1.020	[16]
Abell 2146	2000	120.0	20	74.9	1.602	[17, 18]
Abell 1758N	1500	90.0	15	56.1	1.603	[19, 20]
Abell 115	1600	85.0	15	59.9	1.419	[21, 22]
A3667	1100	45.0	10	41.2	1.092	[23, 24]

The reported statistics are

$$\text{Pearson}(d_{\rm obs}, v_{\rm col}) = 0.925 \quad (p = 3.5 \times 10^{-4}), \tag{32}$$

$$\chi^2/N = \frac{1}{N}\sum_i \left(\frac{d_{{\rm pred},i} - d_{{\rm obs},i}}{\sigma_{d,i}}\right)^2 = 2.46, \tag{33}$$

$$\langle d_{\rm obs}/d_{\rm pred}\rangle = 1.31 \pm 0.10. \tag{34}$$

Including the typical 20–30% systematic dispersion in the literature collision velocities broadens the prediction band and gives $\chi^2/\text{dof} = 1.82$ for the fixed-τ prediction, compared with 3.99 for a constant-offset null.

C Weak-Lensing Covariance and Projection Amplitude

The weak-lensing fits use the Brouwer et al. public data products [25] and their full published covariance matrices. For a data vector $\mathbf{g}_{\rm obs}$ and model $\mathbf{g}_{\rm model}$,

$$\chi^2 = (\mathbf{g}_{\rm obs} - \mathbf{g}_{\rm model})^T C^{-1} (\mathbf{g}_{\rm obs} - \mathbf{g}_{\rm model}). \tag{35}$$

The baryonic-only null is $\mathbf{g}_{\rm model} = \mathbf{g}_{\rm bar}$. The frozen constitutive closure is Eq. (5); no lensing-specific scale is fitted.

Table 5: Primary weak-lensing holdout results.

Sample	χ^2/N (TIDE)	PTE (TIDE)	χ^2/N (baryons)
GAMA isolated	1.22	0.25	6.51
KiDS isolated	7.75	9.8×10^{-18}	110.60

The projection-amplitude audit fits

$$g_{\rm lens} = g_{\rm bar} + A_{\rm rel}\, q(g_{\rm bar}). \tag{36}$$

The fit gives $A_{\rm rel}^{\rm GAMA} = 1.145 \pm 0.127$ and $A_{\rm rel}^{\rm KiDS} = 1.267 \pm 0.032$. The latter corresponds to $\Delta A_{\rm rel} = 0.267 \pm 0.032$, an 8.5σ excess over the scalar closure amplitude.

D Covariant Lensing Closure and Metric-Potential Audit

D.1 Minimal covariant residual metric

Let U be the scalar potential associated with the constitutive residual and let u^μ define the local rest frame of the effective geometric medium. At first order in U, locality and spatial isotropy permit only two independent rank-two deformations,

$$\delta g^{(q)}_{\mu\nu} = AU u_\mu u_\nu + BU h_{\mu\nu}, \qquad h_{\mu\nu} = g_{\mu\nu} + u_\mu u_\nu. \tag{37}$$

Defining U operationally through the non-relativistic acceleration fixes $A = -2$. The remaining ratio is written as $B = -2(2\beta_{\mathrm{W}} - 1)$, giving

$$\delta g^{(q)}_{\mu\nu} = -2U\left[u_\mu u_\nu + (2\beta_{\mathrm{W}} - 1)h_{\mu\nu}\right]. \tag{38}$$

A nonlinear covariant completion with the same linear limit is the disformal metric

$$\widetilde{g}_{\mu\nu} = e^{-2(2\beta_{\mathrm{W}}-1)U} h_{\mu\nu} - e^{2U} u_\mu u_\nu. \tag{39}$$

At $U = 0$, $\widetilde{g}_{\mu\nu} = g_{\mu\nu}$. Expanding Eq. (39) recovers Eq. (38). The residual scalar obeys

$$\tau_{\mathrm{eff}} u^\alpha \nabla_\alpha U + U = U_{\mathrm{eq}}, \qquad q_\mu = -h_\mu{}^\nu \nabla_\nu U. \tag{40}$$

For $ds^2 = a^2[-(1+2\Psi)d\eta^2 + (1-2\Phi)d\mathbf{x}^2]$, Eqs. (38) and (39) yield

$$\Psi_q = U, \qquad \Phi_q = (2\beta_{\mathrm{W}} - 1)U, \qquad \frac{\Phi_q + \Psi_q}{2} = \beta_{\mathrm{W}} U. \tag{41}$$

Timelike geodesics measure U, while convergence and shear measure $\beta_{\mathrm{W}} U$; hence $A_{\mathrm{rel}} = \beta_{\mathrm{W}}$.

D.2 Equivalent stress closure

Using the quasi-static conventions

$$k^2 \Psi_q = -4\pi G a^2 \delta\rho_q, \tag{42}$$

$$k^2(\Phi_q - \Psi_q) = 12\pi G a^2 \Pi_q, \tag{43}$$

the metric relation $\Phi_q = (2\beta_{\mathrm{W}} - 1)\Psi_q$ is equivalent to

$$\boxed{\Pi_q = -\frac{2}{3}(\beta_{\mathrm{W}} - 1)\delta\rho_q.} \tag{44}$$

The sign follows the explicit conventions in Eqs. (42)–(43). At fixed curvature contrast, the physical result is a definite relation between residual density and anisotropic stress. A scalar perfect fluid has $\Pi_q = 0$ and therefore $A_{\mathrm{rel}} = 1$; the measured halo value $A_{\mathrm{rel}} > 1$ requires a non-perfect geometric sector, as naturally provided by a vector or torsional realization.

D.3 Curvature-activated optical operator

Write the torsional mode as $S^\mu = \bar{S} u^\mu + s^\mu$ with $u_\mu s^\mu = 0$. Spatial isotropy forbids a background s^μ, and the electric Weyl tensor $E_{\mu\nu} = C_{\mu\alpha\nu\beta} u^\alpha u^\beta$ vanishes identically on FLRW. The leading local parity-even coupling that produces a directional optical stress is

$$\mathcal{L}_{\mathrm{W}} = \frac{\lambda_{\mathrm{W}}}{2} E_{\mu\nu} s^\mu s^\nu. \tag{45}$$

The operator in Eq. (45) is therefore cubic in first-order perturbations, $E_{\mu\nu}s^\mu s^\nu = \mathcal{O}(\epsilon^3)$. Its field-equation contribution begins at nonlinear order. This is the covariant origin of the separation found numerically between the linear CMB and halo-lensing regimes.

The covariant curvature contrast is

$$\mathcal{W} \equiv \frac{\mathcal{E}^2}{\mathcal{R}_{\rm iso}^2}, \qquad \mathcal{E}^2 = E_{\mu\nu}E^{\mu\nu}, \qquad \mathcal{R}_{\rm iso}^2 = (R_{\mu\nu}u^\mu u^\nu)^2 + \frac{1}{3}(h^{\mu\nu}R_{\mu\nu})^2. \tag{46}$$

It compares trace-free tidal curvature with the locally isotropic Ricci curvature. The minimal response

$$\mathcal{A}_{\rm W}(\mathcal{W}) = \frac{\mathcal{W}}{1+\mathcal{W}} \tag{47}$$

is zero in conformally flat geometry and tends to unity in a Weyl-dominated region. Substitution in Eq. (44) gives

$$\Pi_q = -\frac{2}{3}\alpha_{\rm W}\mathcal{A}_{\rm W}(\mathcal{W})\,\delta\rho_q. \tag{48}$$

Thus the optical amplitude is a response function, not a universal constant.

D.4 Halo matching

The full isolated KiDS sample gives the population-average result

$$A_{\rm rel} = 1.2674 \pm 0.0315, \qquad \left.\frac{\Phi_q}{\Psi_q}\right|_{\rm KiDS} = 1.5348 \pm 0.0631. \tag{49}$$

The three upper stellar-mass bins are mutually consistent and yield the saturated estimate

$$\alpha_{\rm W} = 0.2951 \pm 0.0335, \qquad \left.\frac{\Pi_q}{\delta\rho_q}\right|_{\rm sat} = -0.1967 \pm 0.0224. \tag{50}$$

The lowest-mass bin lies 2.26σ below this plateau after the published cross-bin covariance is included.

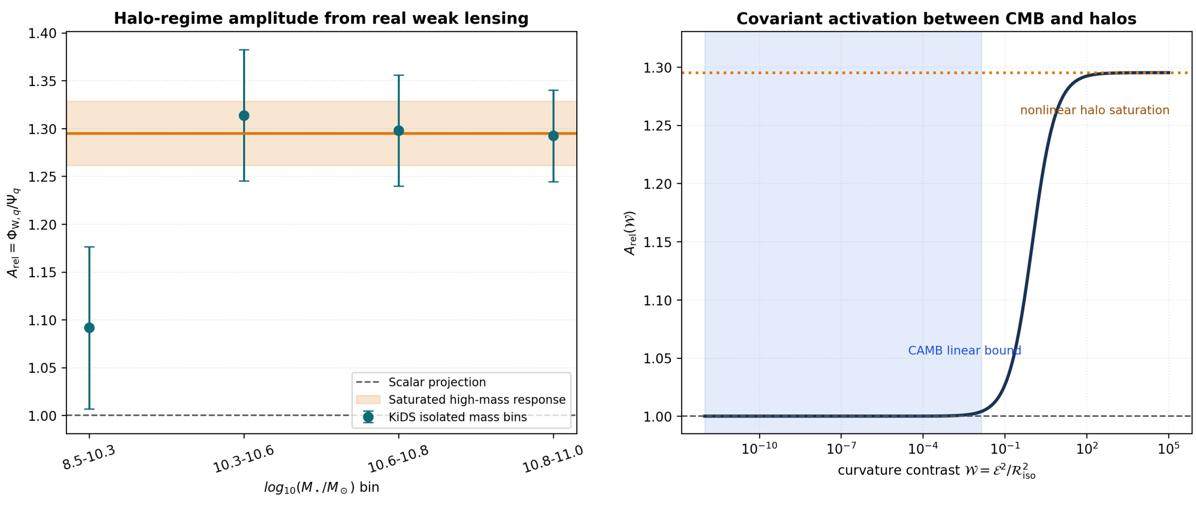

Figure 7: Curvature-activated optical response. Left: full-covariance amplitudes in the four isolated KiDS stellar-mass bins; the upper three define the saturated halo response. Right: the minimal covariant interpolation between conformally flat linear geometry and the Weyl-dominated halo limit. The blue region is the direct CAMB bound on linear leakage of the saturated response.

D.5 Full Einstein–Boltzmann implementation

The source-response patch used in the intermediate likelihood evolves

$$x_c' = -kz + \frac{a}{\tau_{\rm eff}}(\beta_{\rm tide} x_b - x_c). \tag{51}$$

The full optical audit separately defines $x_q = x_c - x_b$ and adds Eq. (44) to CAMB's traceless spatial Einstein equation. In CAMB variables the inserted terms are

$$\delta(g\pi)_{\rm TIDE} = -\frac{2}{3}(\beta_{\rm W} - 1)\rho_c x_q, \tag{52}$$

$$[\delta(g\pi)_{\rm TIDE}]' = -\frac{2}{3}(\beta_{\rm W} - 1)\rho_c (x_q' - 3\mathcal{H} x_q). \tag{53}$$

The null value $\beta_{\rm W} = 1$ recovers the source-response solver with an absolute $\chi^2_{\rm TT}$ difference of 1.9×10^{-7}. Scanning a constant linear $\beta_{\rm W}$ gives

$$\beta_{\rm W}^{\rm best} = 1.000807, \qquad \beta_{\rm W} \in [0.997691, 1.003955] \quad (\Delta\chi^2_{\rm TT} \le 1). \tag{54}$$

The unscreened halo value gives $\Delta\chi^2_{\rm TT} = 6669.4$. Expressed as a fraction of the saturated halo amplitude, the $\Delta\chi^2 = 1$ bound is

$$\mathcal{A}_{\rm W}^{\rm linear} < 1.34 \times 10^{-2}. \tag{55}$$

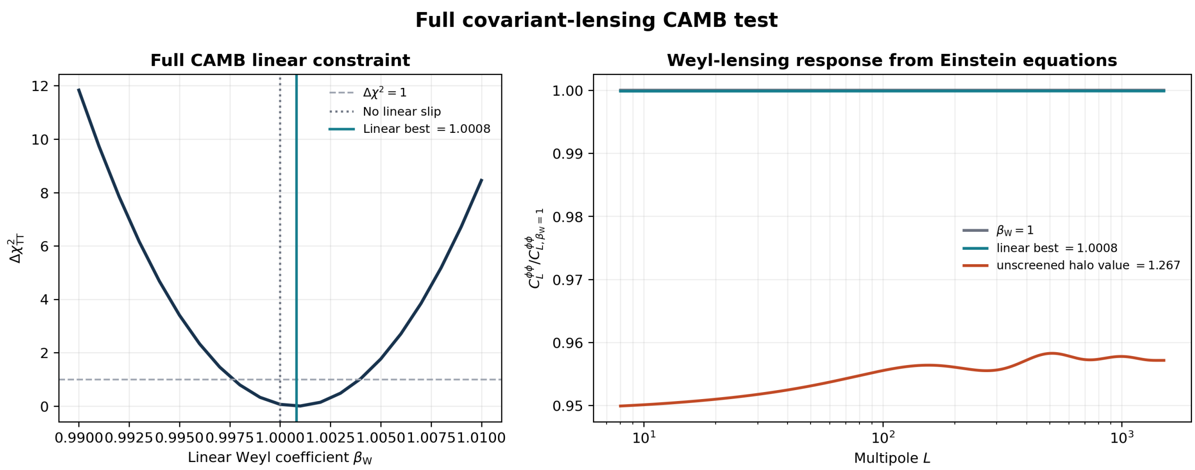

Figure 8: Direct CAMB implementation of the covariant anisotropic-stress closure. Left: Planck TT response to a constant linear $\beta_{\rm W}$. Right: the corresponding Weyl-lensing response. The calculation recovers the unmodified optical sector at $\beta_{\rm W} = 1$ and excludes applying the saturated halo amplitude as an unscreened linear-cosmology coefficient.

The numerical proximity between the intermediate source coefficient $\beta_{\rm tide} \simeq 1.192$ and the KiDS optical amplitude remains an empirical clue, but the completed calculation shows that they act in different equations. The present EFT derives the optical operator and its nonlinear activation. Weak lensing measures its saturated Wilson coefficient $\alpha_{\rm W}$; fixing that number from the microscopic torsional action requires a UV matching calculation beyond the infrared theory used here. In particular, the Proca–Rayleigh sector of Appendix A fixes the relaxation combination Γ_S/m_S^2 but not the optical coupling $\lambda_{\rm W}$. Consequently, neither τ nor dimensional analysis alone can predict the number 0.295: the present derivation establishes its covariant meaning, activation law, and observational matching.

E Peculiar-Velocity Environmental Audit

The 6dFGSv audit uses galaxy-level peculiar velocities from the Fundamental Plane catalogue [26, 27]. The working sample applies $D_H = 40$–200 Mpc and $\epsilon_d < 0.13$, leaving $N = 5292$ galaxies. Local environment is measured by density estimators within $R = 5, 8, 10$ Mpc and galaxies are partitioned into quartiles Q_1–Q_4.

At $R = 8$ Mpc the headline statistic is

$$\sigma(Q_1)/\sigma(Q_4) = 1.232\,[1.206, 1.260], \tag{56}$$

with the 68% interval obtained by bootstrap resampling after trimming the top 5% of $|v_{\rm pec}|$. The Mann–Whitney test gives $p = 6.5 \times 10^{-32}$. The sign persists at $R = 5$ and 10 Mpc:

$$\sigma(Q_1)/\sigma(Q_4) = 1.159,\ 1.232,\ 1.295. \tag{57}$$

A permutation null gives $p < 1/5000$ for the observed Spearman trend. Finally, a partial regression of $\log(|v_{\rm pec}| + 50)$ on distance, distance error and $\log(n_8 + 1)$ gives

$$\beta(\log n_8) = -0.1436, \qquad p = 6.2 \times 10^{-14}, \qquad \Delta\mathrm{AIC} = 54.3. \tag{58}$$

F Native Planck Posterior Audit

The native likelihood run was performed with Cobaya and CAMB 1.6.7 using Planck 2018 low-ℓ TT, SROLL2 low-ℓ EE, Plik-lite high-ℓ TTTEEE, and reconstructed CMB lensing. Both branches sample H_0, $\Omega_b h^2$, $\Omega_c h^2$, $\tau_{\rm reio}$, A_s, and n_s with identical flat priors; $m_\nu = 0.06$ eV, $\Omega_k = 0$, and $r = 0$ are fixed. TIDE additionally samples $-4 < p < 1$ and $0.70 < \beta_{\rm tide} < 1.70$, while $\tau_0 = 11.22$ Mpc/c remains fixed.

Two independent chains were run for each model. All four terminated automatically under the pre-specified criteria $R - 1 < 0.02$ and $R_{\rm cl} - 1 < 0.10$:

$$(R-1)_{\Lambda\mathrm{CDM}} = (0.01458, 0.01641), \qquad (R-1)_{\mathrm{TIDE}} = (0.01560, 0.01800). \tag{59}$$

An independent two-chain GetDist calculation gives $R - 1 = 0.00692$ for ΛCDM and 0.02399 for TIDE, with more than 1400 effective samples for every sampled TIDE parameter. The latter is an orthogonalized cross-chain diagnostic and is distinct from Cobaya's automatic stopping test. Splitting each retained chain by accumulated weight moves no posterior mean by more than 0.09σ (below 0.04σ for p and 0.07σ for $\beta_{\rm tide}$).

After discarding the first 20% of accumulated chain weight, the posterior constraints are those listed in Table 6. The posterior correlation is $\mathrm{corr}(p, \beta_{\rm tide}) = -0.0156$. The lower tail of p

Table 6: Converged native-Planck posterior for the two constitutive parameters. The clock normalization is fixed to the SPARC value.

Parameter	68% interval	95% interval
p	$-2.424^{+1.343}_{-1.094}$	$[-3.923, -0.475]$
$\beta_{\rm tide}$	$1.0128^{+0.0326}_{-0.0356}$	$[0.9392, 1.0791]$

remains limited by the prior boundary, while $\beta_{\rm tide}$ is localized around unity. Across the shared cosmological parameters, the largest shift in posterior means is 0.190σ. At the native minimum, extending the likelihood slice through $p = (-4, -6, -8)$ changes χ^2 by at most 0.27; the archived script reproduces this prior-tail audit.

The profile minima are $\chi^2 = 1005.3374$ for ΛCDM and 1005.2914 for TIDE, corresponding to $\Delta\chi^2 = -0.046$ and $\Delta\mathrm{AIC} = +3.954$. Thus Planck does not reward the two additional constitutive parameters, but it places the fixed-SPARC-clock model on the same likelihood surface with a converged, finite posterior. The exact chains, checkpoints, best-fit files, and post-processing script are included in the reproducibility package.

G Joint CAMB Cosmology Audit

The CAMB-level diagnostic uses the synchronous-gauge CDM contrast slot x_c as an effective clustering channel and adds a relaxation term coupling it to the baryon contrast x_b,

$$\dot{x}_c = -kz + \frac{a}{\tau_{\rm eff}(a)} \left(\beta_{\rm tide} x_b - x_c\right), \qquad \tau_{\rm eff}(a) = \tau_0 a^p. \tag{60}$$

In this audit, x_c and $\Omega_c h^2$ retain CAMB's CDM bookkeeping while the added term tests the constitutive relaxation dynamics at perturbative level. The calculation is therefore not yet a covariant replacement of the background dark-sector stress-energy. The implementation is in synchronous gauge and leaves the baryon continuity and Euler equations unchanged. Both branches were evaluated with CAMB 1.6.7 at $\ell_{\rm max} = 2500$. The joint data vector contains 83 Planck 2018 binned TT points [28], 12 DESI 2024 BAO entries with their full covariance, 1580 Pantheon+ supernovae with the statistical and systematic covariance and analytically marginalized magnitude intercept, and eight $f\sigma_8$ measurements.

Two model branches were sampled: vanilla ΛCDM with five parameters and TIDE with $\tau_0 = 11.22$ Mpc/c fixed while $(p, \beta_{\rm tide})$ were sampled. Flat bounds were used: $55 < H_0 < 80$, $0.019 < \Omega_b h^2 < 0.026$, $0.08 < \Omega_c h^2 < 0.16$, $0.90 < n_s < 1.05$, $2.70 < \ln(10^{10} A_s) < 3.40$, $-4 < p < 1$, and $0.70 < \beta_{\rm tide} < 1.70$. The extended chains used 24 walkers and a 400-step burn-in, retaining 1975 total steps for ΛCDM and 1994 for fixed-τ_0 TIDE. Eight parallel processes were used during sampling.

Table 7: Best sampled χ^2 contributions in the intermediate joint cosmological run.

Model	TT	BAO	Pantheon+	$f\sigma_8$	Total
ΛCDM	81.31	16.93	1388.73	4.57	1491.54
TIDE fixed	63.39	15.74	1389.06	11.44	1479.63

Mean acceptance fractions are 0.548 and 0.472 for ΛCDM and fixed TIDE. Their integrated autocorrelation estimates are 42–46 and 57–74 steps, respectively. Split $\widehat{R}$ reaches 1.032–1.050 for ΛCDM and 1.047–1.075 for fixed TIDE; the corresponding TIDE effective sample counts are 517–669 per parameter. The remaining departure from the strict $\widehat{R} \leq 1.05$ target is concentrated in the broad $(p, \beta_{\rm tide})$ sector and does not shift the posterior location between chain halves. A definitive posterior still requires the full non-lite Planck nuisance treatment together with the expanded cross-probe likelihood. The scripts, HDF5 chains, JSON summaries, trace plots, corner plots, and exact CAMB source tree are included in the reproducibility package.

References

[1] Mordehai Milgrom. A modification of the newtonian dynamics as a possible alternative to the hidden mass hypothesis. *The Astrophysical Journal*, 270:365–370, 1983. doi: 10.1086/161130.

[2] Benoit Famaey and Stacy S. McGaugh. Modified newtonian dynamics (mond): Observational phenomenology and relativistic extensions. *Living Reviews in Relativity*, 15:10, 2012. doi: 10.12942/lrr-2012-10.

[3] Erik P. Verlinde. Emergent gravity and the dark universe. *SciPost Physics*, 2:016, 2017. doi: 10.21468/SciPostPhys.2.3.016.

[4] Federico Lelli, Stacy S. McGaugh, and James M. Schombert. Sparc: Mass models for 175 disk galaxies with spitzer photometry and accurate rotation curves. *The Astronomical Journal*, 152:157, 2016. doi: 10.3847/0004-6256/152/6/157.

[5] Stacy S. McGaugh, Federico Lelli, and James M. Schombert. Radial acceleration relation in rotationally supported galaxies. *Physical Review Letters*, 117:201101, 2016. doi: 10.1103/PhysRevLett.117.201101.

[6] Friedrich W. Hehl, Paul von der Heyde, G. David Kerlick, and James M. Nester. General relativity with spin and torsion: Foundations and prospects. *Reviews of Modern Physics*, 48:393–416, 1976. doi: 10.1103/RevModPhys.48.393.

[7] Ilya L. Shapiro. Physical aspects of the space-time torsion. *Physics Reports*, 357:113–213, 2002. doi: 10.1016/S0370-1573(01)00030-8.

[8] Will Barker and Sebastian Zell. Einstein-proca theory from the einstein-cartan formulation. *Physical Review D*, 109:024007, 2024. doi: 10.1103/PhysRevD.109.024007.

[9] Douglas Clowe, Maruša Bradač, Anthony H. Gonzalez, Maxim Markevitch, Scott W. Randall, Christine Jones, and Dennis Zaritsky. A direct empirical proof of the existence of dark matter. *The Astrophysical Journal Letters*, 648:L109–L113, 2006. doi: 10.1086/508162.

[10] Maxim Markevitch, Anthony H. Gonzalez, Douglas Clowe, Alexey Vikhlinin, William Forman, Christine Jones, Stephen Murray, and Wallace Tucker. Direct constraints on the dark matter self-interaction cross section from the merging galaxy cluster 1e 0657–56. *The Astrophysical Journal*, 606:819–824, 2004. doi: 10.1086/383178.

[11] M. James Jee, John P. Hughes, Felipe Menanteau, Cristóbal Sifón, Rachel Mandelbaum, L. Felipe Barrientos, Leopoldo Infante, and Karen Y. Ng. Weighing "el gordo" with a precision scale: Hubble space telescope weak-lensing analysis of the merging galaxy cluster act-cl j0102-4915 at z = 0.87. *The Astrophysical Journal*, 785:20, 2014. doi: 10.1088/0004-637X/785/1/20.

[12] Felipe Menanteau, John P. Hughes, Cristóbal Sifón, Matt Hilton, Jorge González, Leopoldo Infante, L. Felipe Barrientos, et al. The atacama cosmology telescope: Act-cl j0102–4915 "el gordo", a massive merging cluster at redshift 0.87. *The Astrophysical Journal*, 748:7, 2012. doi: 10.1088/0004-637X/748/1/7.

[13] Maruša Bradač, Steven W. Allen, Tommaso Treu, Harald Ebeling, Richard Massey, R. Glenn Morris, Anja von der Linden, and Douglas Applegate. Revealing the properties of dark matter in the merging cluster macs j0025.4-1222. *The Astrophysical Journal*, 687:959–967, 2008. doi: 10.1086/591246.

[14] M. James Jee, Henk Hoekstra, Andisheh Mahdavi, and Arif Babul. Hubble space telescope/advanced camera for surveys confirmation of the dark substructure in a520. *The Astrophysical Journal*, 783:78, 2014. doi: 10.1088/0004-637X/783/2/78.

[15] Douglas Clowe, Maxim Markevitch, Maruša Bradač, Anthony H. Gonzalez, S. M. Chung, Richard Massey, and Dennis Zaritsky. On dark peaks and missing mass: A weak-lensing mass reconstruction of the merging cluster abell 520. *The Astrophysical Journal*, 758:128, 2012.

[16] Nathan Golovich, Reinout J. van Weeren, William A. Dawson, M. James Jee, and David Wittman. Mc^2: Multi-wavelength and dynamical analysis of the merging galaxy cluster zwcl 0008.8+5215: An older and less massive bullet cluster. *The Astrophysical Journal*, 838: 110, 2017. doi: 10.3847/1538-4357/aa6670.

[17] H. R. Russell, J. S. Sanders, A. C. Fabian, S. A. Baum, M. Donahue, A. C. Edge, B. R. McNamara, and C. P. O'Dea. Chandra observation of two shock fronts in the merging galaxy cluster abell 2146. *Monthly Notices of the Royal Astronomical Society*, 406:1721–1733, 2010. doi: 10.1111/j.1365-2966.2010.16822.x.

[18] Lindsay J. King, Douglas I. Clowe, Joseph E. Coleman, Helen R. Russell, et al. The distribution of dark and luminous matter in the unique galaxy cluster merger abell 2146. *Monthly Notices of the Royal Astronomical Society*, 459:517–527, 2016. doi: 10.1093/mnras/stw507.

[19] Brian Ragozzine, Douglas Clowe, Maxim Markevitch, Anthony H. Gonzalez, and Marusa Bradac. A weak-lensing study of the merging galaxy cluster abell 1758. *The Astrophysical Journal*, 2012.

[20] Rogério Monteiro-Oliveira, Eduardo S. Cypriano, Rubens E. G. Machado, Gastão B. Lima Neto, André L. B. Ribeiro, Laerte Jr. Sodré, and Renato A. Dupke. The merger history of the complex cluster abell 1758: A combined weak-lensing and spectroscopic view. *Monthly Notices of the Royal Astronomical Society*, 466:2614–2632, 2017. doi: 10.1093/mnras/stw3238.

[21] Mincheol Kim, M. James Jee, Kyle Finner, Nathan Golovich, William A. Dawson, David Wittman, et al. Multiwavelength analysis of the merging galaxy cluster abell 115. *The Astrophysical Journal*, 874:143, 2019. doi: 10.3847/1538-4357/ab0d7c.

[22] Nathan Golovich, William A. Dawson, David Wittman, M. James Jee, et al. Merging cluster collaboration: Optical and spectroscopic survey of a radio-selected sample of merging galaxy clusters. *The Astrophysical Journal Supplement Series*, 240:39, 2019.

[23] Alexis Finoguenov, Craig L. Sarazin, Kazuhiro Nakazawa, Daniel R. Wik, and Tracy E. Clarke. Deep xmm-newton observations of the northwest radio relic region of abell 3667. *The Astrophysical Journal*, 715:1143–1156, 2010.

[24] Matt S. Owers, Warrick J. Couch, Paul E. J. Nulsen, and Scott W. Randall. Substructure in the cold front cluster abell 3667. *The Astrophysical Journal*, 693:901–914, 2009. doi: 10.1088/0004-637X/693/1/901.

[25] M. M. Brouwer et al. The weak-lensing radial acceleration relation: Constraining modified gravity and cold dark matter theories with kids-1000. *Astronomy & Astrophysics*, 650:A113, 2021. doi: 10.1051/0004-6361/202040108.

[26] Lachlan A. Campbell, John R. Lucey, Matthew Colless, D. Heath Jones, Christopher M. Springob, Christina Magoulas, Robert N. Proctor, Jeremy R. Mould, Mike A. Read, Sarah Brough, Tom Jarrett, Alex I. Merson, Philip Lah, Florian Beutler, Michelle E. Cluver, and Quentin A. Parker. The 6df galaxy survey: Fundamental plane data. *Monthly Notices of the Royal Astronomical Society*, 443(2):1231–1251, 2014. doi: 10.1093/mnras/stu1198.

[27] Christopher M. Springob, Christina Magoulas, Matthew Colless, Jeremy Mould, Pirin Erdoğdu, D. Heath Jones, John R. Lucey, Lachlan Campbell, and Christopher J. Fluke. The 6df galaxy survey: peculiar velocity field and cosmography. *Monthly Notices of the Royal Astronomical Society*, 445(3):2677–2697, 2014. doi: 10.1093/mnras/stu1743.

[28] Planck Collaboration, N. Aghanim, et al. Planck 2018 results. vi. cosmological parameters. *Astronomy & Astrophysics*, 641:A6, 2020. doi: 10.1051/0004-6361/201833910.